

# Quantum spin spiral ground state of the ferrimagnetic sawtooth chain

Roman Rausch<sup>1</sup>, Matthias Peschke<sup>2,3</sup>, Cassian Plorin<sup>3</sup>, Jürgen Schnack<sup>4</sup>, Christoph Karrasch<sup>1</sup>

**1** Technische Universität Braunschweig, Institut für Mathematische Physik,  
Mendelssohnstraße 3, 38106 Braunschweig, Germany

**2** Institute for Theoretical Physics Amsterdam and Delta Institute for Theoretical  
Physics, University of Amsterdam, Science Park 904, 1098 XH Amsterdam, The  
Netherlands

**3** Department of Physics, University of Hamburg, Notkestraße 9, D-22607 Hamburg,  
Germany

**4** Faculty of Physics, Bielefeld University, Universitätsstr. 25, 33615 Bielefeld, Germany

\* r.rausch@tu-braunschweig.de

July 17, 2022

## 1 Abstract

The ferrimagnetic phase of the sawtooth chain with mixed ferromagnetic nearest-neighbour interactions  $J$  and antiferromagnetic next-nearest-neighbour interactions  $J'$  (within the isotropic Heisenberg model) was previously characterized as a phase with commensurate order. In this paper, we demonstrate that the system in fact exhibits an incommensurate quantum spin spiral. Even though the ground state is translationally invariant in terms of the local spin expectations  $\langle \mathbf{S}_i \rangle$ , the spiral can be detected via the connected spin-spin correlations  $\langle \mathbf{S}_i \cdot \mathbf{S}_j \rangle - \langle \mathbf{S}_i \rangle \cdot \langle \mathbf{S}_j \rangle$  between the apical spins. It has a long wavelength that grows with  $J'$  and that soon exceeds finite-system sizes typically employed in numerical simulations. A faithful treatment thus requires the use of state-of-the-art simulations for large, periodic systems.

In this work, we are able to accurately treat  $L = 400$  sites (200 unit cells) with periodic boundary conditions using the density-matrix renormalization group (DMRG). This is possible due to the exploitation of the  $SU(2)$  symmetry which results in effective bond dimensions of more than 1,000,000. Our results are corroborated by variational uniform matrix product state (VUMPS) calculations, which work directly in the thermodynamic limit at the cost of a lower accuracy.

---

## 19 Contents

|    |   |          |
|----|---|----------|
| 20 | <b>1 Introduction</b>                         | <b>2</b> |
| 21 | 1.1 Frustration and ferrimagnets              | 2        |
| 22 | 1.2 The sawtooth chain                        | 3        |
| 23 | 1.3 Previous results                          | 4        |
| 24 | <b>2 Technical details</b>                    | <b>5</b> |
| 25 | 2.1 Finite systems                            | 5        |
| 26 | 2.2 Infinite systems                          | 6        |
| 27 | 2.3 Expectation values, spin structure factor | 7        |

|    |  |           |
|----|--|-----------|
| 28 | <b>3 Exemplary case</b> $J = -1, J' = 1$           | <b>10</b> |
| 29 | <b>4 Total spin in the ferrimagnetic phase</b>     | <b>12</b> |
| 30 | <b>5 Static spin structure factor</b>              | <b>15</b> |
| 31 | <b>6 Conclusion</b>                                | <b>17</b> |
| 32 | <b>A Error estimates</b>                           | <b>18</b> |
| 33 | A.1 Energy   | 18        |
| 34 | A.2 Finite system: translation invariance          | 18        |
| 35 | A.3 Infinite systems: error analysis               | 20        |
| 36 | A.4 Comparison between finite and infinite systems | 22        |
| 37 | <b>References</b>                                  | <b>24</b> |

---

38

39

## 40 1 Introduction

### 41 1.1 Frustration and ferrimagnets

42 The Lieb-Mattis theorem [1, 2] states that for a bipartite Heisenberg system with an-  
 43 tiferromagnetically coupled sublattices A and B, the ground state has the total spin  
 44  $|S_{\max,A} - S_{\max,B}|$ , where  $S_{\max,A}$  and  $S_{\max,B}$  are the maximally possible spins of the re-  
 45 spective sublattices. For the common case that the sublattices are equivalent (i.e., consist  
 46 of atoms with the same spin) and are of equal size, this yields a singlet ground state. If  
 47 they are inequivalent, one obtains a ferrimagnet with a predictable ground-state spin and  
 48 opposite orientations of the sublattice polarizations.

49 The situation gets more complicated if frustration is allowed to enter into the picture  
 50 and the couplings become non-bipartite. In addition, mixed ferro- and antiferromagnetic  
 51 couplings can result in a ferrimagnet even for equivalent sublattices. This is the case we  
 52 will consider in this paper.

53 Interacting localized spins are commonly described by the Heisenberg model, which  
 54 can be generally written down as

$$H = \sum_{i<j} J_{ij} \mathbf{S}_i \cdot \mathbf{S}_j, \quad (1)$$

55 where  $\mathbf{S}_i = (S_i^x, S_i^y, S_i^z)$  is the spin operator at site  $i$  and  $J_{ij}$  are the coupling constants that  
 56 define the geometry. Since the Heisenberg Hamiltonian commutes with each component  
 57 of the vector of the total spin  $\mathbf{S}_{\text{tot}} = \sum_i \mathbf{S}_i$  as well as with its square,

$$[H, \mathbf{S}_{\text{tot}}^2] = 0, \quad (2)$$

58 there exists a simultaneous eigenbasis of  $H$  and  $\mathbf{S}_{\text{tot}}^2$ , and the ground state can in principle  
 59 take any value of  $S_{\text{tot}}$  between 0 and  $LS$ , where  $L$  is the number of sites and where  $S_{\text{tot}}$   
 60 is determined from

$$\langle \mathbf{S}_{\text{tot}}^2 \rangle = S_{\text{tot}} (S_{\text{tot}} + 1). \quad (3)$$

61 Intuitively, it is clear that for the mixed-coupling case, where  $J_{ij} > 0$  for some sites and  
 62  $J_{ij} < 0$  for others, there should be a region where neither the singlet state  $S_{\text{tot}}/L = 0$ , nor

63 the ferromagnet  $S_{\text{tot}}/L = S$  minimizes the energy and the ground state will have some  
 64 partial polarization  $0 < S_{\text{tot}}/L < S$ . For later purposes, we also introduce the quantum  
 65 number  $M_{\text{tot}}$  related to the conservation of the  $z$ -component, i.e., a U(1) spin symmetry:

$$\langle S_{\text{tot}}^z \rangle = \sum_i \langle S_i^z \rangle = M_{\text{tot}}. \quad (4)$$

66 Since the Lieb-Mattis theorem does not hold anymore in the frustrated case,  $S_{\text{tot}}$   
 67 must be determined from a full many-body calculation. In addition, frustration may  
 68 favour non-collinear spin-spiral or canted states [3–5]. This should be understood in a  
 69 quantum sense: A finite polarization can be interpreted as a spontaneous breaking of the  
 70 SU(2) symmetry down to U(1), with the total spin pointing along the quantization axis.  
 71 Hence, there is no classical non-collinear order, where the angle of the classical vector  
 72  $\langle \mathbf{S}_i \rangle = (\langle S_i^x \rangle, \langle S_i^y \rangle, \langle S_i^z \rangle)$  would vary as a function of the site index  $i$  [6]. However, the  
 73 spin-spin correlations may peak at a value of the wavevector not equal to 0 or  $\pi$ , which  
 74 signals non-collinearity. An alternative diagnostic is the susceptibility to small twists [3, 7].

75 From an experimental perspective, there are several examples of systems with mixed  
 76 ferro- and antiferromagnetic interactions. Some one-dimensional cuprates can be described  
 77 as extended  $S = 1/2$  Heisenberg chains with nearest-neighbour exchange  $J < 0$  and next-  
 78 nearest-neighbour exchange  $J' > 0$  [8–11]. Another case are single-molecule magnets  
 79 (SMM), a subclass of which is based on Mn ions of various sizes and geometries [12]. The  
 80 largest to date are the  $\{\text{Mn}_{70}\}$  and  $\{\text{Mn}_{84}\}$  wheels [13, 14] with  $S = 2$  Mn(III) centres and  
 81 a surprisingly low total spin of  $S_{\text{tot}} = 5 - 8$ . These are finite, but still quite challenging  
 82 systems, which have received thorough theoretical attention only recently [15], pointing  
 83 to a necessity of mixed FM-AFM interactions to achieve such a low spin.

## 84 1.2 The sawtooth chain

85 In this work, we focus on another FM-AFM system, the “sawtooth” or “delta” ( $\Delta$ ) chain  
 86 [3, 5, 16–20], which consists out of vertex-sharing triangles and which is probably the  
 87 simplest 1D geometry with geometrical frustration<sup>1</sup> (see Fig. 1). It features a two-site unit  
 88 cell with alternating “apical” (A) and “basal” (B) spins. The corresponding Heisenberg  
 89 Hamiltonian is given by

$$H = J \sum_i (\mathbf{S}_i^A \cdot \mathbf{S}_i^B + \mathbf{S}_i^A \cdot \mathbf{S}_{i+1}^B) + J' \sum_i \mathbf{S}_i^B \cdot \mathbf{S}_{i+1}^B, \quad (5)$$

90 where the sums run over the unit cells ( $L = 2N_{\text{cells}}$ ).  $J$  and  $J'$  are the exchange coupling  
 91 constants, one of which sets the energy scale. The sawtooth chain comes essentially in two  
 92 variants: An AFM-AFM one with both  $J > 0$  and  $J' > 0$  [21–28]; and a mixed FM-AFM  
 93 one with  $J < 0$  and  $J' > 0$  [5, 17–20].

94 Experimentally, the sawtooth geometry is found for atacamite (AFM-AFM,  $S = 1/2$ ,  
 95  $J'/J \approx 3.29$ ) [29], for the ring molecule  $\text{Fe}_{10}\text{Gd}_{10}$  [30] (FM-AFM, mixed  $S = 5/2$  and  
 96  $S = 7/2$ ,  $J'/|J| \approx 0.65$ ) and for a malonato-bridged Cu complex [17] (FM-AFM,  $S = 1/2$ ,  
 97  $J'/|J| \approx 0.91$ ).

98 In this paper, we investigate the homogeneous FM-AFM  $S = 1/2$  case, relevant for the  
 99 last material. We note that  $J'/|J| \approx 0.91$  [17] is within the interesting region  $J'/|J| \sim 1$ ,  
 100 where the couplings are of equal strength. We will thus pay special attention to the point  
 101  $J'/|J| = 1$  in this work.

<sup>1</sup>While the kagome lattice is also composed out of vertex-sharing triangles, it is complicated by closed loops. The sawtooth chain, on the other hand, is a special case of a delta tree without closed loops [16].

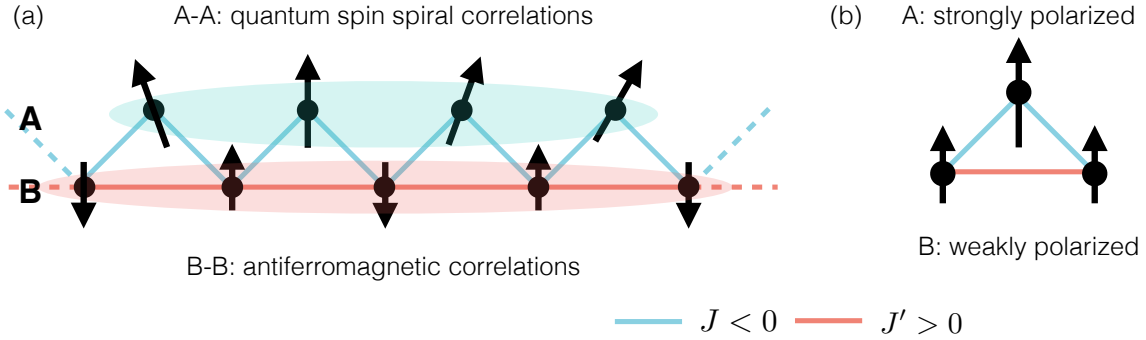


Figure 1: Sketch of the FM-AFM sawtooth chain and the proposed magnetic order in the ferrimagnetic phase. The apical and basal sites are labeled as “A” and “B”, respectively. (a) Schematic visualization of the spin-spin correlations. (b) Visualization of the spin polarization pattern. Both the quantum spin spiral (A-A) and the AFM order (B-B) can only be detected via the connected spin-spin correlations and not via the polarization.

102 If the coupling between the apical spins cannot be neglected, one needs to add the  
 103 corresponding term to the Hamiltonian:

$$H_\gamma = \gamma J' \sum_i \mathbf{S}_i^A \cdot \mathbf{S}_{i+1}^A. \quad (6)$$

104 For  $\gamma = 1$ , the Hamiltonian reduces to an extended Heisenberg chain [31,32]. In this work,  
 105 we only deal with the sawtooth limit  $\gamma = 0$ .

### 106 1.3 Previous results

107 We briefly summarize the state of knowledge regarding the  $S = 1/2$  AFM-AFM sawtooth  
 108 chain. It features three phases as a function of  $J'/J$ , namely gapless antiferromagnetic,  
 109 gapped dimerized, and gapless non-collinear [3]. The non-collinear phase has not been  
 110 much explored to the best of our knowledge; most studies have focused on the dimer-  
 111 ized phase, where a valence-bond solid (VBS) ground state appears for  $J' = J$ , which  
 112 has solitonic excitations [21, 22, 24]. Flat magnon bands appear at the specific point  
 113  $J'/J = 1/2$  [28, 33–35] and lead to an exceptionally large jump from full saturation to half  
 114 saturation due to localized magnons [23, 25–27].

115 We will now recapitulate prior results for the mixed-coupling (FM-AFM)  $S = 1/2$  saw-  
 116 tooth chain, which is the subject of this paper. A first theoretical treatment used exact  
 117 diagonalization (ED) as well as density-matrix renormalization group (DMRG) calcula-  
 118 tions for odd chain lengths  $L = 7, 11, 15, \dots, 31, 47, 67$  [18]. For  $J' = 0$  the system must  
 119 clearly be ferromagnetic (with  $S_{\text{tot}}/L = 1/2$ ), and it is found that ferromagnetism persists  
 120 for small  $J'/|J|$ . A transition to a ferrimagnetic phase is observed for  $J'/|J| = 0.5$ . The  
 121 total spin per site was found to follow  $S_{\text{tot}}/L = (L - 1) / (4L) + 1/2L$  and thus approaches  
 122  $1/4$  for  $L \rightarrow \infty$ . No further statements on the nature of the ground state were given in  
 123 this paper [18].

124 Later works mostly dealt with particular regimes and specific questions such as the  
 125 crossover between the Ising and Heisenberg limits [19], the comparison of magnetization  
 126 curves with the experiment [20], or the thermodynamics around the critical point [36], in  
 127 particular with an application to the ferromagnetic molecule  $\text{Fe}_{10}\text{Gd}_{10}$  [37].

128 Recently, the system received renewed interest, and the properties of the ferrimagnetic  
 129 phase (including the finite- $\gamma$  case) were investigated in great detail using the DMRG

130 for finite systems with open and periodic boundary conditions (exploiting the U(1) spin  
 131 symmetry and using bond dimensions up to  $\chi = 8000$ ) [5]. For  $\gamma = 0$ , previous results [18]  
 132 were confirmed, whereby the total spin per site for even rings up to  $L \sim 50$  is of the form  
 133  $S_{\text{tot}}/L = 1/4 + 1/L$ , implying that  $S_{\text{tot}}/L$  can be extrapolated in the thermodynamic  
 134 limit. The phase was characterized as a commensurate ferrimagnet that only becomes  
 135 incommensurate for  $\gamma > 0$ .

136 In this paper, we revisit the sawtooth chain using DMRG with periodic boundary  
 137 conditions. By exploiting the SU(2) spin symmetry, we can access rings larger by about  
 138 a factor of 10 and come to a different conclusion about the nature of the ground state:  
 139 We find that the total spin takes irrational values  $0.25 \lesssim S_{\text{tot}}/L \lesssim 0.28$  and probably  
 140 reaches  $1/4$  only for  $J' \rightarrow \infty$ . The ground state is characterized by an incommensurate  
 141 quantum spin spiral in the connected apex-apex correlations  $\langle \mathbf{S}_i^A \cdot \mathbf{S}_j^A \rangle - \langle \mathbf{S}_i^A \rangle \cdot \langle \mathbf{S}_j^A \rangle$ .  
 142 The main reason for this discrepancy is that the wavelength of the spiral is generally very  
 143 large; it grows with  $J'$  and soon exceeds finite-system sizes that were considered in prior  
 144 works. Another confounding factor are the very small energy gaps between the various  
 145 spin sectors (in particular for large values of  $J'/|J|$ ), which renders the exploitation of the  
 146 SU(2) symmetry extremely beneficial for this problem.

## 147 2 Technical details

### 148 2.1 Finite systems

149 For finite systems, we use the DMRG algorithm, which is a well-established approach  
 150 to compute ground state properties of 1D problems variationally in the space of matrix-  
 151 product states [38, 39]. Its effectiveness rests on the so-called “area law” for the entangle-  
 152 ment entropy [40], which guarantees a low entanglement for ground states of short-ranged  
 153 Hamiltonians on 1D chains with open boundary conditions, which can be used to truncate  
 154 the full Hilbert space to a much smaller relevant space. The main control parameter of  
 155 this truncation is called the “bond dimension”  $\chi$ . We use the one-site algorithm with a  
 156 subspace expansion method [41] to dynamically increase the bond dimension during the  
 157 iterations and have selectively checked that the two-site algorithm [39] yields the same  
 158 results.

159 It was shown that for the sawtooth chain, the interpretation of results obtained for  
 160 open boundary conditions can be subtle and complicated [5], probably because the Friedel  
 161 oscillations at the open ends interfere with the delicate spin order and the small energy  
 162 gaps. Hence, it is better to use periodic boundary conditions, but this generally diminishes  
 163 the effectiveness of the DMRG and one needs to employ extremely large bond dimensions.  
 164 However, we can counteract this by exploiting the SU(2) symmetry of the problem [42, 43]  
 165 and access very large effective bond dimensions  $\chi_{\text{eff}}$ , while numerically working with a  
 166 much smaller and tractable  $\chi_{\text{SU}(2)} \ll \chi_{\text{eff}}$ .

167 The exploitation of the SU(2) symmetry boils down to using the Wigner-Eckart the-  
 168 orem which states that under SU(2) symmetry, matrix elements only depend on the spin  
 169 projections via Clebsch-Gordan coefficients that can be separated out. This means that  
 170 the local blocks within the DMRG ansatz state effectively correspond to  $2S_{\text{block}} + 1$  states  
 171 for every intermediate value of  $S_{\text{block}}$ . The presence of a finite polarization  $S_{\text{tot}} \neq 0$  offers  
 172 an interesting additional advantage when combined with the SU(2) symmetry: Since the  
 173 total spin is an extensive quantity, merely doubling the system size while keeping  $\chi_{\text{SU}(2)}$   
 174 constant roughly doubles  $\chi_{\text{eff}}$ . However, we find that  $\chi_{\text{SU}(2)}$  should still be further in-  
 175 creased to preserve a high accuracy for the larger system. We can go as high as  $L = 200$

| $L$      | symmetry | $\chi/\chi_{\text{SU}(2)}$ | $\chi_{\text{eff}}$ (rounded) |
|----------|----------|----------------------------|-------------------------------|
| 40       | SU(2)    | 500                        | 10,000                        |
| 60       | SU(2)    | 2000                       | 50,000                        |
| 100      | SU(2)    | 2000                       | 100,000                       |
| 200      | SU(2)    | 2000                       | 200,000                       |
| 252      | SU(2)    | 3000                       | 300,000                       |
| 300      | SU(2)    | 4000                       | 600,000                       |
| 400      | SU(2)    | 6500                       | 1,360,000                     |
| $\infty$ | no symm. | 1000-1200                  | -                             |
| $\infty$ | U(1)     | 3000-4000                  | -                             |
| $\infty$ | SU(2)    | 3000                       | 55,000                        |

Table 1: Typical bond dimensions and system sizes used in this work in terms of the system size  $L$  and the symmetries exploited in the algorithm. For finite systems, we always use periodic boundary conditions. For  $L = \infty$  and the case of SU(2), we can only access the sector  $S_{\text{tot}} = 0$ .

176 without problems, and for selected points even up to  $L = 400$  with periodic boundary  
177 conditions. Table 1 shows the typical bond dimensions used in this work. Large values of  
178  $S_{\text{tot}}$  require a stable computation of Wigner  $3j$  and  $6j$  symbols for large inputs, for which  
179 we use the WIGXJPF library [44].

180 For finite systems, we can directly target any desired value of  $S_{\text{tot}}$ , compute the corre-  
181 sponding lowest energy  $E_0(S_{\text{tot}})$ , and identify the ground state from the minimum. The  
182 error is assessed by computing the variance per site

$$\text{Var}(E)/L = \left( \langle H^2 \rangle - \langle H \rangle^2 \right) / L. \quad (7)$$

183 As we show in App. A.1, this measure is proportional to the actual error in the ground-  
184 state energy density, which allows us to put error bars on the computed energies. In  
185 addition, we can assess the accuracy by comparing with results of Lanczos diagonalization  
186 for smaller system sizes up to  $L = 36$  (see App. A.1).

187 Since the variance per site has the dimension of energy squared and its scale changes  
188 with  $J$  and  $J'$ , we ensure that the largest parameter in the Hamiltonian is of modulus 1:  
189 First, we set  $J = -1$  and increase  $J'$  up to  $J' = 1$ . Then, we keep  $J' = 1$  and let  $J$  go to  
190 zero. Only the ratio  $J'/|J|$  matters for the phase diagram.

191 The main advantage of working with a finite system is the high accuracy of the DMRG  
192 with the SU(2) symmetry. The main disadvantage are the finite-size effects which become  
193 quite severe for the given problem, even for system sizes of  $\mathcal{O}(10^2)$  sites, as will be shown  
194 below.

## 195 2.2 Infinite systems

196 For infinite boundary conditions, we use the variational uniform matrix-product state  
197 (VUMPS) formalism [45, 46], which is based on the time-dependent variational principle  
198 and offers improved efficiency over the original infinite DMRG [38]. Our numerical unit cell  
199 encompasses two physical unit cells (4 sites) in order to allow for AFM order. While finite-  
200 size effects are eliminated, this approach comes at the disadvantage that the exploitation  
201 of symmetries is limited: We can only use  $S_{\text{tot}} = 0$  in the case of SU(2) and only a rational  
202  $M_{\text{tot}}$  within the unit cell in the case of U(1). Since the finite-system data indicates that  
203 the physical ground state is generally not a spin singlet, we can thus not employ the highly  
204 efficient SU(2) numerics.

205 If  $U(1)$  symmetries are exploited in the infinite system, there is to the best of our  
 206 knowledge no practical way to compute the value of  $S_{\text{tot}}/L$ . In order to access  $S_{\text{tot}}/L$ , we  
 207 switch off the symmetry altogether [47]. Within the degenerate set of  $2S_{\text{tot}} + 1$  states, the  
 208 DMRG tends to converge to the state with  $M_{\text{tot}} = S_{\text{tot}}$  whose entanglement is minimal. In  
 209 this case,  $\langle S_i^{z,\alpha} \rangle$  and  $\langle S_i^{x,\alpha} \rangle$  ( $\alpha = A, B$ ) take finite, translationally invariant values ( $\langle S_i^{y,\alpha} \rangle$   
 210 vanishes by time-reversal symmetry), and we can compute  $S_{\text{tot}}$  from

$$S_{\text{tot}}^\alpha/N_{\text{cells}} = \sqrt{\langle S_i^{x,\alpha} \rangle^2 + \langle S_i^{z,\alpha} \rangle^2}, \quad S_{\text{tot}}/L = (S_{\text{tot}}^A/N_{\text{cells}} + S_{\text{tot}}^B/N_{\text{cells}})/2. \quad (8)$$

211 As an error estimate for infinite systems, we look at the convergence with respect to the  
 212 bond dimension  $\chi$  (see App. A.3).

### 213 2.3 Expectation values, spin structure factor

214 A polarized ground state has a  $(2S_{\text{tot}} + 1)$ -fold degeneracy, and one needs to specify w.r.t. to  
 215 which of these states expectation values are computed. Within the  $SU(2)$ -symmetric  
 216 approach for the finite system, we can directly access each member of the multiplet [42, 43].  
 217 In the infinite system, one can straightforwardly only determine the state with  $M_{\text{tot}} = 0$   
 218 using the  $U(1)$ -symmetric algorithm or the state with  $M_{\text{tot}} = S_{\text{tot}}$  if no symmetries are  
 219 exploited.

220 In order to demonstrate the existence of a quantum spin spiral, we want to compute  
 221 the static spin structure factor, i.e., the Fourier transform of the spin-spin correlations.  
 222 For a local operator  $O_i^\alpha$ , we define the connected correlation function as

$$\langle O_j^\alpha O_l^\beta \rangle_c = \langle O_j^\alpha O_l^\beta \rangle - \langle O_j^\alpha \rangle \langle O_l^\beta \rangle. \quad (9)$$

223 For the specific case of a ring with an even, finite number of unit cells  $N_{\text{cells}}$ , the static  
 224 spin structure factor is obtained as follows:

$$\begin{aligned} C^{\alpha\beta}[O](k) &= \frac{1}{N_{\text{cells}}} \sum_{j,l=-N_{\text{cells}}/2+1}^{N_{\text{cells}}/2} e^{ik(j-l)} \langle O_j^\alpha O_l^\beta \rangle_c \\ &= \sum_{l=-N_{\text{cells}}/2+1}^{N_{\text{cells}}/2} e^{ik(j_0-l)} \langle O_{j_0}^\alpha O_l^\beta \rangle_c \\ &= \langle O_{j_0}^\alpha O_{j_0}^\beta \rangle_c + e^{ikN_{\text{cells}}/2} \langle O_{j_0}^\alpha O_{j_0+N_{\text{cells}}/2}^\beta \rangle_c \\ &\quad + \sum_{d=1}^{N_{\text{cells}}/2-1} \left[ e^{ikd} \langle O_{j_0}^\alpha O_{j_0+d}^\beta \rangle_c + e^{-ikd} \langle O_{j_0}^\alpha O_{j_0-d}^\beta \rangle_c \right]. \end{aligned} \quad (10)$$

225 We have assumed translational invariance, so that the result is independent of the site  $j_0$ ,  
 226 and have rewritten the summations in terms of the distance  $d$ . In the infinite system, one  
 227 can evaluate the same equation for  $N_{\text{cells}} \rightarrow \infty$ , which on a technical level is achieved by  
 228 using the MPS transfer matrix [46]. For  $\alpha = \beta$ , real matrix elements, and neglecting the  
 229 second term that extends across the whole system, Eq. (10) reduces to a cosine transform:

$$C^{\alpha\alpha}[O](k) \approx \langle O_{j_0}^\alpha O_{j_0}^\alpha \rangle_c + 2 \sum_{d=1}^{N_{\text{cells}}/2-1} \cos(kd) \langle O_{j_0}^\alpha O_{j_0+d}^\alpha \rangle_c. \quad (11)$$

230 In the finite case with  $SU(2)$  symmetry being exploited, we compute<sup>2</sup>

$$C^{\alpha\beta}[\mathbf{S}] = C^{\alpha\beta}[S^x] + C^{\alpha\beta}[S^y] + C^{\alpha\beta}[S^z], \quad (12)$$

231 and  $k$  can only take discrete values  $k = 2\pi n/N_{\text{cells}}$  with  $n = 0, 1, \dots, N_{\text{cells}} - 1$ . Due to the  
 232  $SU(2)$  symmetry of the problem, the first term in Eq. (9) is independent of  $M_{\text{tot}}$  for the  
 233 vector-vector correlations. In order to subtract the correct asymptotic value (and avoid  
 234 a divergence at  $k = 0$ ), the second term is evaluated for  $M_{\text{tot}} = S_{\text{tot}}$ . In the infinite case  
 235 with  $U(1)$  symmetry being exploited, we compute

$$\lim_{N_{\text{cells}} \rightarrow \infty} C^{\alpha\beta}[S^z], \quad (13)$$

236 where  $k$  can take continuous values. In this case, both terms in Eq. (9) depend on the  
 237 choice of  $M_{\text{tot}}$ , while we can only access the sector  $M_{\text{tot}} = 0$ . However, we observe that  
 238 the first term in Eq. (9) does not take a finite asymptotic value and that the second term  
 239 vanishes (see Sec. A.4 and Fig. 15).

240 While the two correlation functions in Eqs. (12) and (13) do not coincide exactly,  
 241 they can both be used to demonstrate the existence of a spin spiral and to determine its  
 242 wavevector  $k_{\text{peak}} \neq 0, \pi$ .

---

<sup>2</sup>Note that within the  $SU(2)$ -symmetric approach, the question of accessing individual  $x, y, z$ -components of either  $\langle \mathbf{S}_j^\alpha \cdot \mathbf{S}_l^\beta \rangle$  or  $\langle \mathbf{S}_j^\alpha \rangle$  becomes meaningless. Technical details can be found in Refs. [42, 43].



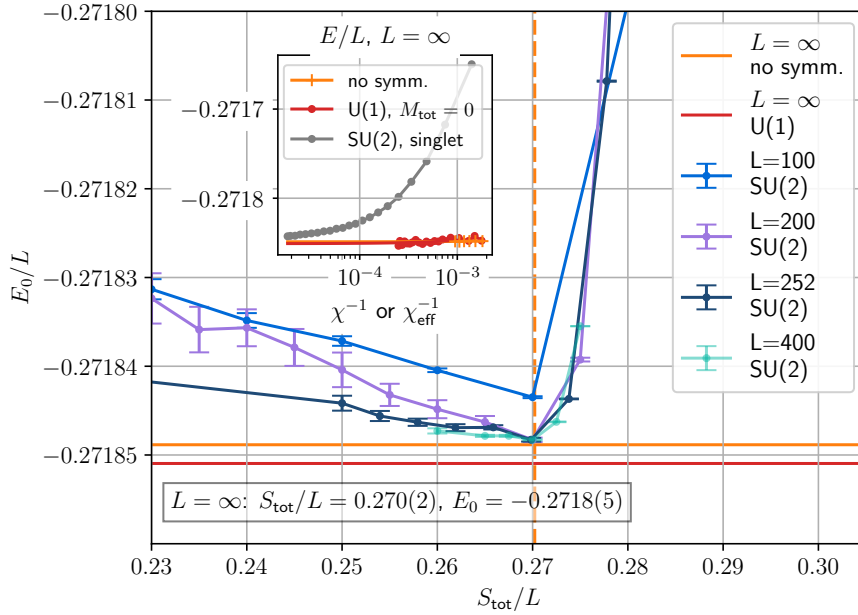


Figure 2: Lowest energies of the sawtooth chain with  $J = -1$ ,  $J' = 1$  in various sectors of the total spin  $S_{\text{tot}}$  for finite systems, obtained using the SU(2)-symmetric DMRG with periodic boundary conditions. The lowest energy among the sectors is compared with the infinite-system (VUMPS) calculations, where one cannot target a specific sector of  $S_{\text{tot}}$  (horizontal lines). The vertical dotted line shows  $S_{\text{tot}}/L$  computed according to Eq. 8 for the infinite system without symmetries. The respective bond dimensions can be found in Tab. 1, and the estimation of error bars is outlined in App. A.1. The inset shows the energy as a function of the inverse bond dimension  $\chi^{-1}$  or the inverse effective bond dimension  $\chi_{\text{eff}}^{-1}$  as an error estimate for the case of infinite systems (solid lines are inter/extrapolations).

### 243 3 Exemplary case $J = -1, J' = 1$

244 Figure 2 shows the energy profile  $E_0(S_{\text{tot}})$  for finite systems (compared with the infinite  
 245 one) in the interesting case of  $J = -1, J' = 1$ . For finite systems, the total spin per site  
 246 must be rational, and we find the lowest-energy state (i.e., the true ground state) in the  
 247 sector  $S_{\text{tot}}/L = 27/100$  for  $L = 100, 200$  and in the sector  $S_{\text{tot}}/L = 68/252$  for  $L = 252$ .  
 248 In all cases, these are the closest possible rational values to 0.270, so that this result seems  
 249 converged w.r.t. the system size. The infinite-system result (without symmetries) appears  
 250 to be irrational, and to the leading digits we obtain  $S_{\text{tot}}/L \approx 0.270(2)$ . Thus, our results  
 251 are not in agreement with  $S_{\text{tot}}/L = 1/4$  that was obtained before [5, 18], motivating a  
 252 deeper investigation.

253 The ground-state energies are in good agreement between the finite- and infinite-system  
 254 calculations (both for the case that no symmetry and that U(1) symmetry is exploited). In  
 255 the curve  $E_0(S_{\text{tot}})/L$ , we observe a steep barrier towards high spins and a much shallower  
 256 barrier towards small spins, where the energy density  $E_0/L$  varies only in the fifth digit  
 257 after the decimal point for the system sizes considered. Moreover, the energy gaps become  
 258 smaller with larger system sizes, indicating gapless excitations, but only with respect to a  
 259 decrease of the total spin.

260 It is notable that large, macroscopic changes in the total spin have very small gaps.  
 261 Even the sector  $S_{\text{tot}} = 0$  is very close in energy to the ground state, as was noticed  
 262 before [5]; the inset of Fig. 2 shows that the singlet energy approaches the ground-state  
 263 energy for large bond dimensions. This is, however, not an effect of frustration and is  
 264 already observed for the FM Heisenberg chain<sup>3</sup>.

265 From a technical point of view, the small gaps render the determination of the total  
 266 spin very difficult unless SU(2) symmetries are exploited. Many low-lying states with  
 267  $S_{\text{tot}} \neq 0$ , but  $M_{\text{tot}} = 0$  are expected to compete if only  $M_{\text{tot}} = 0$  is fixed, but they are  
 268 projected out exactly if  $S_{\text{tot}}$  is fixed. This may contribute to the discrepancy between our  
 269 results and previous works.

---

<sup>3</sup>For the FM Heisenberg chain, the total spin needs no calculation, as one can analytically show that it is maximal [48].

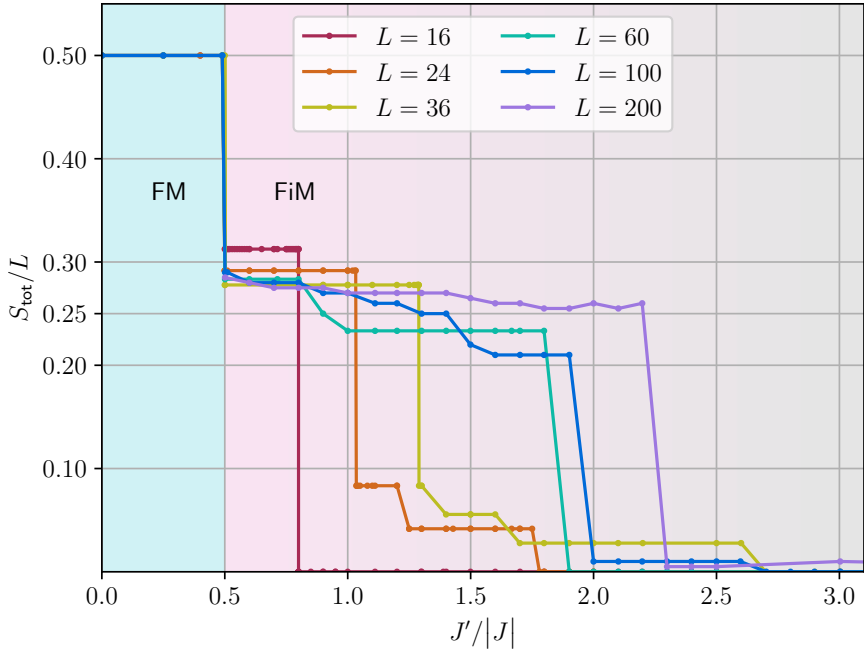


Figure 3: Total ground-state spin per site  $S_{\text{tot}}/L$  for various finite systems with periodic boundary conditions. For  $L \leq 36$ , the results were obtained using exact diagonalization (Lanczos algorithm). For the other values, we used the DMRG with  $SU(2)$  symmetries and identified the true ground state from the minimum of  $E_0(S_{\text{tot}})$  similarly to Fig. 2. FM and FiM denote the ferromagnetic and ferrimagnetic phase, respectively.

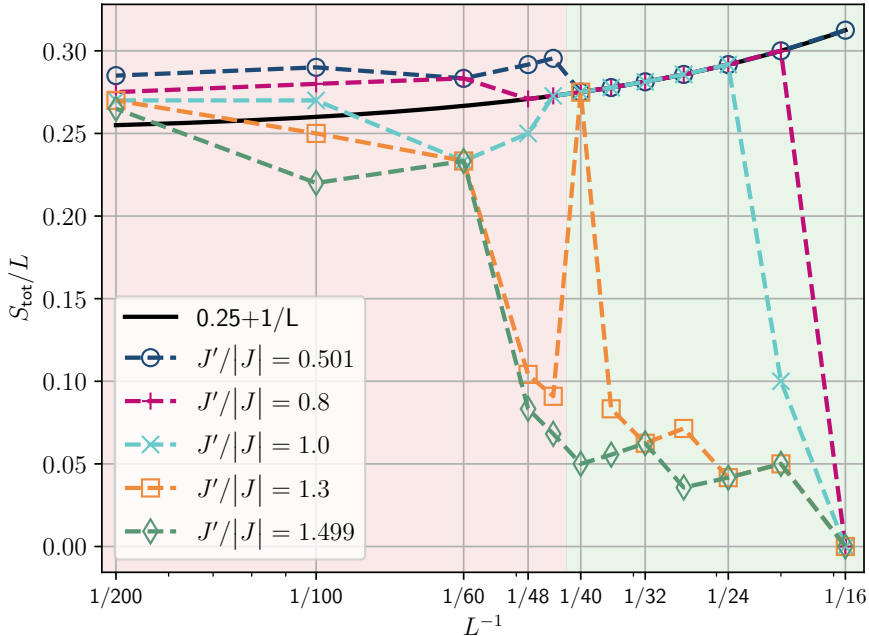


Figure 4: The same as Fig. 3 but plotted as a function of the inverse system size  $L^{-1}$  for various values of  $J'/|J|$ . The curve  $f(L^{-1}) = 0.25 + L^{-1}$  is shown for comparison. For small  $J'/|J|$ , the points collapse to  $f(L^{-1})$  for a certain range of  $L$  (green area), but this is not the case for larger  $L$  or larger  $J'/|J|$  (red area).

## 270 4 Total spin in the ferrimagnetic phase

271 We now study the behaviour when moving away from the point  $J = -1$ ,  $J' = 1$ . Figure 3  
 272 shows  $S_{\text{tot}}/L$  as a function of  $J'/|J|$  for different system sizes. The transition from the  
 273 ferromagnet  $S_{\text{tot}}/L = 1/2$  to the ferrimagnet at  $J'/|J| = 0.5$  is unambiguous.

274 At the quantum critical point  $J'/|J| = 0.5$ , the DMRG finds that all values of the  
 275 total spin are degenerate within the numerical accuracy, whereas Lanczos (as well as full  
 276 SU(2) diagonalization for smaller systems) indicates that only the values  $S_{\text{tot}} = L/2, L/2 -$   
 277  $1, \dots, L/4, 0$  are degenerate.

278 In the ferrimagnetic phase, we observe the following features: (a) After crossing the  
 279 quantum critical point,  $S_{\text{tot}}/L$  jumps discontinuously to a value slightly above (but dif-  
 280 ferent from) 0.25. (b) One can reach convergence for  $S_{\text{tot}}/L$  w.r.t. the accessible system  
 281 size up to  $J'/|J| \lesssim 1$ . (c) For  $J'/|J| \gtrsim 1$  it appears that we cannot access systems that  
 282 are large enough to obtain convergence, and  $S_{\text{tot}}/L$  features plateaus at various values of  
 283 the spin. In particular,  $S_{\text{tot}}/L$  at some point jumps to a low-spin state  $0.005 \sim 0.01$  and  
 284 eventually to zero. (d) The value of  $J'/|J|$  where this jump happens increases with the  
 285 system size.

286 The chaotic behaviour with respect to the system size already points towards incom-  
 287 mensurate behaviour, while the observation (d) suggests that the low-spin state is a finite-  
 288 size effect. We investigate these questions in more detail below.

289 In order to shed light on the discrepancy between our data and prior results, we  
 290 now plot the same data as a function of  $1/L$  in an attempt to perform an extrapolation  
 291 w.r.t. the system size (see Fig. 4), as was done in Refs. [5, 18]. One observes that for  
 292 not too large  $J'/|J|$ , the points start collapsing on the curve  $S_{\text{tot}}/L = 1/4 + 1/L$ , which  
 293 makes it tempting to extrapolate  $S_{\text{tot}}/L = 1/4$  in the thermodynamic limit. However, if  
 294 we increase the system size further instead of extrapolating, we find that the behaviour  
 295 becomes chaotic somewhere around  $L = 44$ . For  $J'/|J| \gtrsim 1.5$ , the results in fact do not  
 296 fall on  $S_{\text{tot}}/L = 0.25 + 1/L$  at all. In both cases, this indicates that an intrinsic length  
 297 scale is surpassed, and this length scale increases with  $J'/|J|$ . It is thus essential to access  
 298 systems larger than this length scale (green area of Fig. 4). This is probably the main  
 299 reason for the discrepancy between our results and previous works.

300 Next, we compare the behaviour of large, finite systems  $L = 100, 200$  with results  
 301 obtained directly in the thermodynamic limit via the VUMPS algorithm (see Fig. 5).  
 302 One finds that the infinite-system result for  $S_{\text{tot}}/L$  is in good agreement with the one for  
 303  $L = 100$  up to  $J'/|J| \approx 1$  and with the one for  $L = 200$  up to  $J'/|J| \approx 1.5$  (and still in  
 304 moderate agreement up to  $J'/|J| \approx 2.2$ ). The crosses in the plot indicate energetically  
 305 close sectors of the total spin for the finite system, illustrating again that the energy  
 306 minimum is extremely shallow. Finite-size wavering within these minima is thus not  
 307 surprising. One also notices that a second shallow minimum ( $S_{\text{tot}}/L \sim 0.01$ ) develops  
 308 around  $J'/|J| \gtrsim 2$  at very low spins and eventually becomes the absolute one. This jump  
 309 to low spins is not found in the infinite system. Thus, we concur with Ref. [5] that this  
 310 jump is most likely a finite-size effect.

311 One should note that for  $J'/|J| = \infty$  (equivalent to  $J = 0$ ,  $J' = 1$ ), the apical spins  
 312 become free spins. Thus, the ground state is degenerate for all values of  $S_{\text{tot}}/L = 0 \dots 1/4$   
 313 [18]. This raises the question what the effect of an infinitesimal  $J < 0$  is. Our numerical  
 314 methods are ill-posed to answer this question because any gap will also be infinitesimal.  
 315 Nevertheless, we note the following: The inset of Fig. 5 displays the polarization of the  
 316 apical and basal spins for the infinite system computed without symmetries, i.e., in the  
 317 sector  $M_{\text{tot}} = S_{\text{tot}}$ . The polarization is translationally invariant, i.e.,  $\langle S_i^{\alpha,x} \rangle$  and  $\langle S_i^{\alpha,z} \rangle$   
 318 are independent of  $i$  within numerical inaccuracies (in the sector  $M_{\text{tot}} = 0$ , one finds

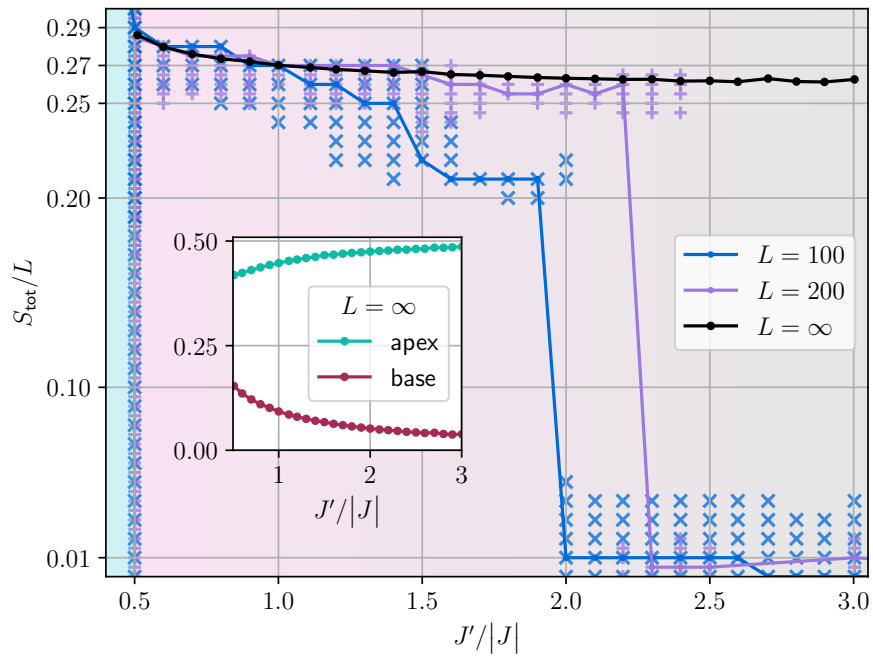


Figure 5: The same as Fig. 3, but including DMRG data obtained for the infinite system (VUMPS) without exploiting symmetries. In addition, the crosses indicate sectors of  $S_{\text{tot}}$  in the finite system for which the energy density is within  $10^{-3}$  of the ground-state energy density, illustrating the extreme shallowness of the energy minima (cf. Fig. 6). The inset shows the (translationally invariant) apical and basal polarization  $\sqrt{\langle S_i^{x,\alpha} \rangle^2 + \langle S_i^{z,\alpha} \rangle^2}$  ( $\alpha = A, B$ ) for  $L = \infty$ .

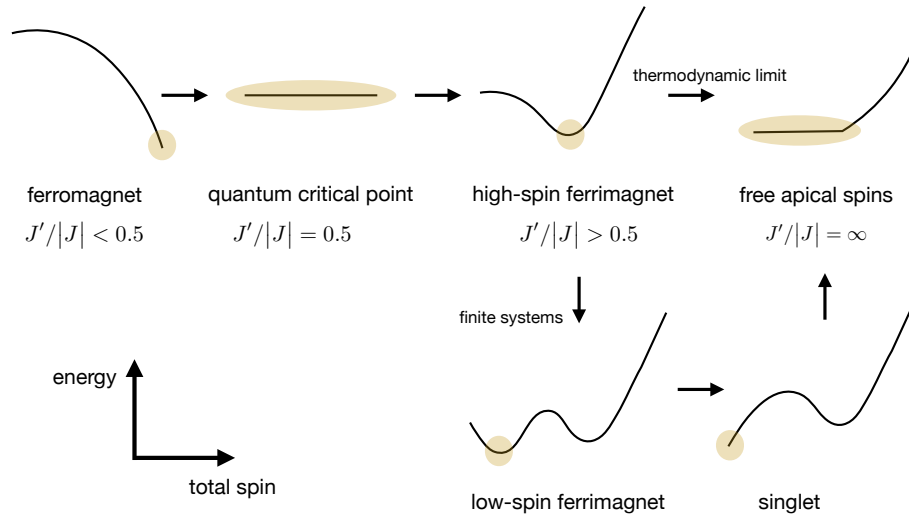


Figure 6: Schematic representation of the energy landscape  $E(S_{\text{tot}})$ . The parameter  $J'/|J|$  is increasing from left to right. The yellow blob indicates the absolute energy minimum. The curves are all exaggerated and the real minima are much more shallow (see Fig. 2).

For  $J'/|J| < 0.5$ , the system is a ferromagnet with maximal spin. At the quantum critical point  $J'/|J| = 0.5$ , we find that  $E(S_{\text{tot}})$  is completely flat and that all  $S_{\text{tot}}$  values are degenerate for large  $L$  within the numerical accuracy (see Fig. 5). For  $J'/|J| > 0.5$ , we find a ferrimagnet with  $0.25 \lesssim S_{\text{tot}}/L \lesssim 0.28$ . For finite systems, a low-spin minimum appears if  $J'/|J|$  is increased further. Eventually this minimum flattens out and the ground state becomes a singlet. Such a singlet ground state is not found in the thermodynamic limit. Finally, for  $J'/|J| = \infty$ , the apical spins become free spins and the ground state is degenerate for the values  $0 \leq S_{\text{tot}}/L \leq 1/4$ .

319  $\langle S_i^{z,A} \rangle \approx \langle S_i^{z,B} \rangle \approx 0$ ), which we can also confirm for finite systems. We see that the  
 320 apical spins get more and more polarized towards  $1/2$ , while the basal spins approach 0.  
 321 This suggests that in the limit  $J'/|J| \rightarrow \infty$ , one approaches  $S_{\text{tot}}/L = 1/4$  very slowly.  
 322 However, since the infinite-system calculations become progressively more difficult, we  
 323 are only able to reliably treat  $J'/|J| = 3 \sim 4$  and cannot exclude the possibility that  
 324 additional effects happen for larger values.

325 Figure 6 is a schematic summary of the findings discussed in this chapter.

## 326 5 Static spin structure factor

327 Next, we demonstrate the existence of a quantum spin spiral. We first note that such a  
 328 spiral cannot be detected from the polarization alone since the ground state is transla-  
 329 tionally invariant (up to numerical errors). In the sector  $M_{\text{tot}} = S_{\text{tot}}$ , the expectations  
 330  $\langle \mathbf{S}_i^A \rangle$  and  $\langle \mathbf{S}_i^B \rangle$  take values which do not depend on the cell index  $i$ ; for  $M_{\text{tot}} = 0$ , we have  
 331  $\langle \mathbf{S}_i^A \rangle = \langle \mathbf{S}_i^B \rangle = 0$ . Thus, we compute the static spin structure factor, and we perform the  
 332 calculation both in the finite and infinite system<sup>4</sup>. The results are shown in Figs. 7 and 8.

333 Figure 7 shows the apex-apex structure factor  $C^{AA}[\mathbf{S}]$  for various finite  $L$  and  $J = -1$ ,  
 334  $J' = 1$ . It features a peak at a small non-zero value of the momentum, and conver-  
 335 gence w.r.t the system size can be reached. For the largest systems of  $L = 300, 400$ , we  
 336 find  $k_{\text{peak}} = 14/150\pi \approx 0.093\pi$  and  $k_{\text{peak}} = 18/200\pi \approx 0.090\pi$ . This corresponds to a  
 337 wavelength of  $\lambda_{\text{cells}} = 2\pi/k_{\text{peak}} \approx 21.4 \sim 22.2$  unit cells or  $\lambda = 2\lambda_{\text{cells}} \approx 42.9 \sim 44.4$  sites.

338 While the largest system sizes of  $L = 200, 300, 400$  all yield very similar results, there  
 339 are strong outliers in the smaller systems: For  $L = 60$  (inset), we find  $k_{\text{peak}} = 4/30\pi \approx$   
 340  $0.13\pi$  or  $\lambda = 30$  sites, so that slightly decreasing the wavelength to a value that is com-  
 341 mensurate with the system size seems to be energetically favourable. The peak becomes  
 342 much sharper.

343 Figure 8 shows  $C^{AA}[S^z]$  in the infinite system with a continuous  $k$  and for different  
 344 values of  $J'/|J| = 1$ . For  $J'/|J| = 1$ , we find  $k_{\text{peak}} \approx 0.097\pi$  in agreement with the finite-  
 345 size calculation. The peak moves closer to zero as  $J'/|J|$  is increased. At  $J'/|J| = 3$ ,  
 346 we have  $k_{\text{peak}} \approx 0.048$  and thus roughly a doubled wavelength of about  $\lambda \approx 82.8$  sites as  
 347 compared with  $J'/|J| = 1$ . We note that the correlations between the basal spins simply  
 348 remain antiferromagnetic, with a sharp  $k_{\text{peak}} = \pi$  (see the left inset of Fig. 8).

349 In summary, we conclude that the apex spins form a quantum spin spiral with a  
 350 very long wavelength that increases with  $J'/|J|$ . Thus, finite-size rings only reflect the  
 351 behaviour in the thermodynamic limit as long as  $L$  accommodates at least several wave-  
 352 lengths. Quantitatively, we find that at least  $L \gtrsim 2.5\lambda$  is necessary. This again illustrates  
 353 that one needs to access large systems and explains the discrepancy with prior results.

354 In Fig. 9, we study the structure factor for a fixed system size of  $L = 100$  as  $J'/|J|$   
 355 is increased beyond  $J'/|J| = 1$ . At  $J'/|J| = 1.4$ , we see that a second peak develops  
 356 at the smallest possible non-zero  $k$ -value of  $2\pi/50 = 0.04\pi$  ( $\lambda = 100$ ) in addition to the  
 357 main peak at  $6\pi/50 = 0.12\pi$ . For  $J'/|J| = 1.5$ , the main peak shifts to  $4\pi/50 = 0.08\pi$   
 358 ( $\lambda = L/2 = 50$ ), which coincides with the plateau above  $S_{\text{tot}}/L \gtrsim 0.2$  in Fig. 5. Finally,  
 359 the spiral collapses completely at  $J'/|J| = 2$  in favor of pure ferromagnetic alignment  
 360 with  $k_{\text{peak}} = 0$ . This means that as soon as the wavelength of the spiral becomes too  
 361 large, finite-size spirals that form a ‘‘standing wave’’ on the ring with  $\lambda = L$  or  $\lambda = L/2$   
 362 start to compete. Eventually, collinear alignment becomes energetically favourable and  
 363 the spiral breaks down. This coincides with the jump to a low-spin state in Figs. 3 and 5,

<sup>4</sup>We reiterate that the spin structure factor is defined differently in both cases and partially depends on the choice of  $M_{\text{tot}}$ . Details can be found in Sec. 2.3

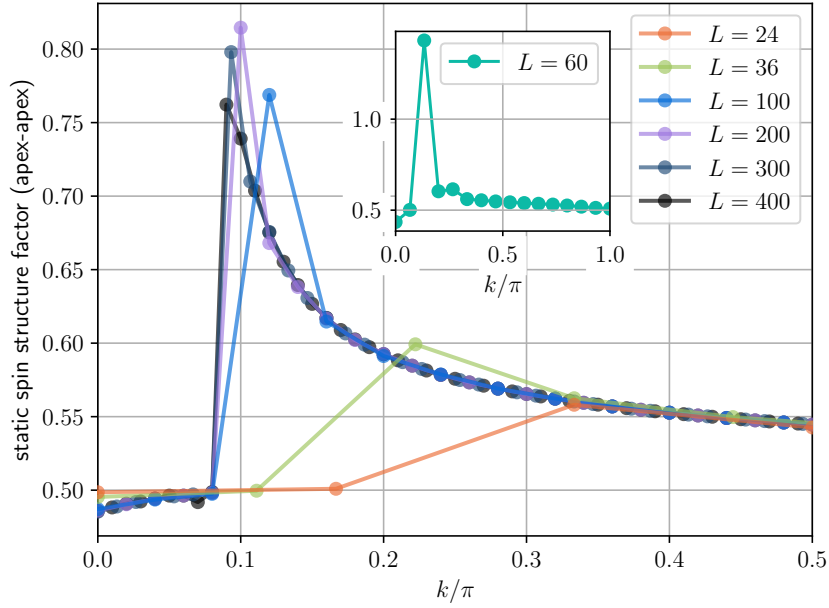


Figure 7: Static apex-apex spin-structure factor as a function of the momentum  $k$  for finite systems with periodic boundary conditions and  $J = -1$ ,  $J' = 1$  (Eqs. (11) and (12) with  $\alpha = \beta = A$ ).

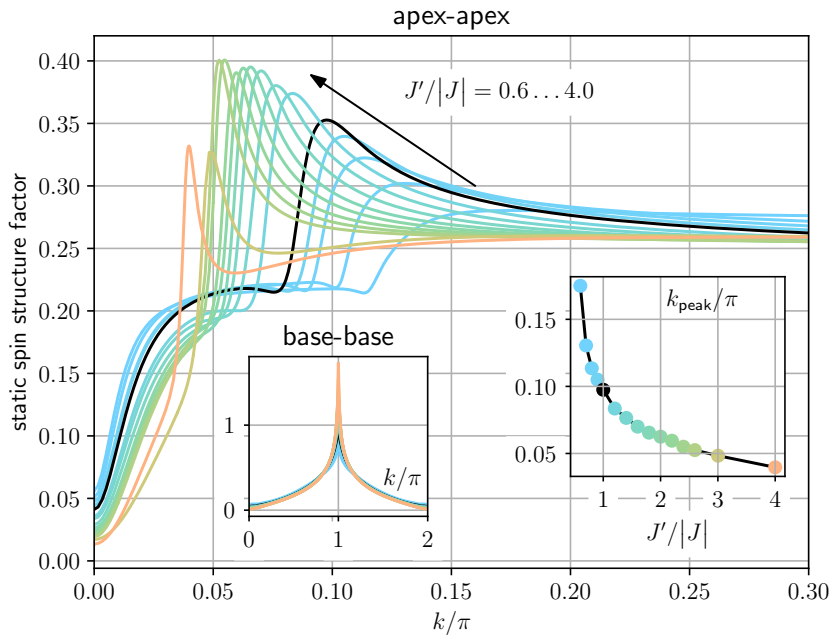


Figure 8: Static apex-apex spin-structure factor for the infinite system with the  $U(1)$  spin symmetry exploited (Eqs. (10) and (13) with  $\alpha = \beta = A$ ). The right inset shows the position of the peak as a function of  $J'/|J|$  with the same colours as the main plot. The left inset shows the corresponding base-base structure factor ( $\alpha = \beta = B$ ).



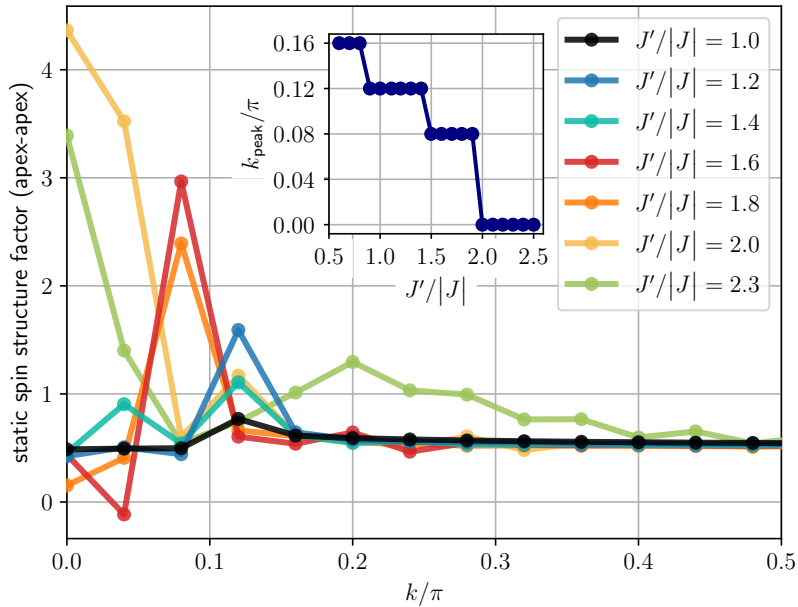


Figure 9: The same as Fig. 7, but for a fixed system size of  $L = 100$  and different values of  $J'/|J|$ . The inset shows the position of the main peak as a function of  $J'/|J|$ .

364 giving more evidence that the low-spin plateau is a finite-size effect: The long-wavelength  
 365 quantum spin spiral breaks down in a finite system that is too small to host it. In other  
 366 words, the value of the total spin is related to the wavevector of the spiral; we observe  
 367 that the long-wavelength spiral is only favorable in combination with a large polarization  
 368 of  $0.25 \lesssim S_{\text{tot}}/L \lesssim 0.28$ .

## 369 6 Conclusion

370 We have demonstrated that the ground state of the FM-AFM sawtooth chain with  $J'/|J| >$   
 371  $0.5$  is a ferrimagnet that features an incommensurate quantum spin spiral for the apical  
 372 spins as well as ordinary antiferromagnetic correlations between the basal spins. The in-  
 373 commensurate behaviour is seen in the spin-spin correlations, while the ground state itself  
 374 is translationally invariant.

375 The wavelength of the spiral is large and grows with  $J'/|J|$ , quickly exceeding sizes  
 376  $L = 20 - 60$  that are used in typical finite-size calculations (with periodic boundary  
 377 conditions). By exploiting the  $SU(2)$  spin symmetry within our DMRG approach, we are  
 378 able to accurately treat systems of  $L = 200 - 400$  sites with effective bond dimensions in  
 379 the range of  $10^5 - 10^6$ . Using the VUMPS formalism, we can tackle the infinite system  
 380 without finite-size effects at the cost of a lower accuracy. The two methods complement  
 381 each other and corroborate the above conclusion.

382 Finally, we have argued that the low-spin plateau found for the FM-AFM sawtooth  
 383 chain is a finite-size effect related to the competition of the incommensurate infinite-  
 384 system spiral with finite-system spirals of wavelength  $\lambda = L, L/2$ . An intriguing question  
 385 is whether the same physics underlies the Mn wheels (as well as related magnetic molecules  
 386 [12]), which are finite systems of 70-84 magnetic centres [13–15] and which also exhibit  
 387 a low-spin ground state stemming from from mixed FM-AFM exchange couplings [15].  
 388 In particular, one may wonder whether or not the low-spin state in these systems is also

389 connected to quantum spin spirals with wavelengths spanning across the whole molecule.

390 Overall, the FM-AFM sawtooth chain presents an interesting example of the caveats  
391 that come with an extrapolation in the system size. Of course, we cannot fully exclude  
392 the possibility that additional effects appear on even larger length scales beyond what has  
393 been considered here.

394 An open question for future work is how our observations are affected by an additional  
395 apex-apex coupling  $\gamma \neq 0$  (see Eq. (6)) or if the case of AFM-AFM couplings also features  
396 similar incommensurate behaviour, in particular when polarized by magnetic fields [29].

## 397 Acknowledgements

398 R.R. and C.K. acknowledge support by the Deutsche Forschungsgemeinschaft (DFG, Ger-  
399 man Research Foundation) through the Emmy Noether program (KA3360/2-1) as well as  
400 by ‘Niedersächsisches Vorab’ through the ‘Quantum- and Nano-Metrology (QUANOMET)’  
401 initiative within the project P-1.

402 M.P. is funded by the Deutsche Forschungsgemeinschaft (DFG, German Research  
403 Foundation) – project ID 497779765.

404 C.P. is supported by the Deutsche Forschungsgemeinschaft (DFG) through the Cluster  
405 of Excellence Advanced Imaging of Matter – EXC 2056 – project ID 390715994.

406 J.S. is funded by the Deutsche Forschungsgemeinschaft (DFG, German Research Foun-  
407 dation) - project ID 449703145 as well as by the Leibniz Supercomputing Center in Garch-  
408 iving - project ID pr62to.

## 409 A Error estimates

### 410 A.1 Energy

411 In order to translate the energy variance per site (Eq. (7)) into an actual error bar for the  
412 energy, we compute the ground state for different energy variances per site and compare  
413 with the result of exact diagonalization for  $L = 36$  (see Fig. 10).

414 The typical range of values for the variance that we can achieve for large systems is  
415  $\text{Var}(E)/L \sim 10^{-8} - 10^{-5}$ . We find that in this regime, the variance is linearly related to  
416 the true error  $\epsilon$ :

$$\epsilon \sim 0.337 \text{Var}(E)/L. \quad (14)$$

417 The prefactor may of course depend on both  $J'/|J|$  and  $L$ , but Fig. 10 illustrates that  
418 it is roughly the same for  $J'/|J| = 0.9$  and  $J'/|J| = 2$ . By comparing with exact-  
419 diagonalization results for  $L = 16$  (not shown) we find that the relationship still holds.

420 Thus, we assume that Eq. (14) is generally valid, at least as an order-of-magnitude  
421 estimate. This allows us to put error bars  $\pm\epsilon$  on the energy densities shown in Fig. 2. In all  
422 calculations in this paper, we choose the bond dimension such that  $\text{Var}(E)/L \leq \mathcal{O}(10^{-6})$   
423 around the minimum of  $E_0(S_{\text{tot}})$ .

### 424 A.2 Finite system: translation invariance

425 We can check to which extent the ground state of the finite system with periodic boundary  
426 conditions is in fact translationally invariant. To this end, we compute  $\langle \mathbf{S}_i^A \rangle$  and  $\langle \mathbf{S}_i^B \rangle$  (for  
427  $M_{\text{tot}} = S_{\text{tot}}$ ) and quantify their spread using the standard deviation of the distribution for  
428 all choices  $i = 1, 2 \dots N_{\text{cells}}$ . We reiterate that within the SU(2)-symmetric approach, it  
429 becomes meaningless to ask for the individual component, one obtains  $\langle \mathbf{S}_i^{A,B} \rangle$  as a scalar

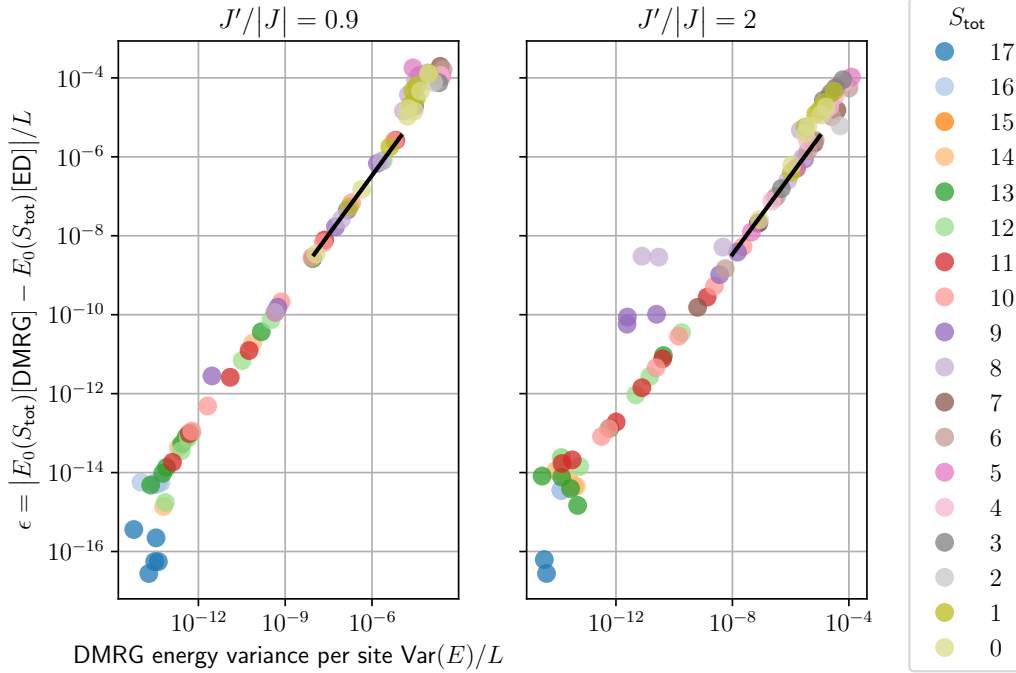


Figure 10: Comparison of the energy density  $E_0/L$  computed using DMRG with the exact-diagonalization (ED) result obtained via spinpack [49] for  $L = 36$ ,  $J'/|J| = 0.9$  (left) and  $J'/|J| = 2$  (right), for various values of the total spin  $S_{\text{tot}}$ . The DMRG results are computed for different bond dimensions  $\chi_{\text{SU}(2)}$ , which corresponds to different energy variances per site (see Eq. (7)). The black line is a linear fit, see Eq. (14). For  $J'/|J| = 2$  and  $S_{\text{tot}} = 8, 9$  we were only able to achieve an agreement within  $\epsilon \sim 10^{-10} - 10^{-9}$ .

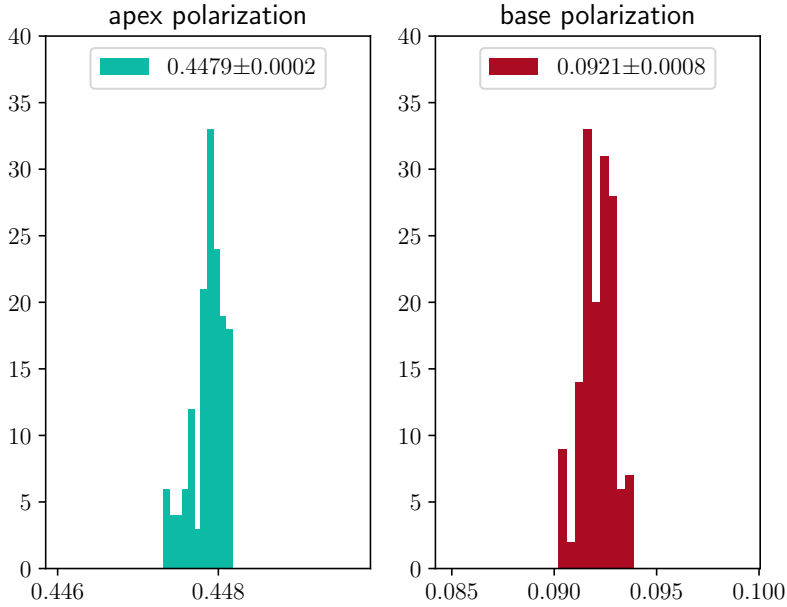


Figure 11: Histogram of the spin polarization  $\langle \mathbf{S}_i^A \rangle$  (apex) and  $\langle \mathbf{S}_i^B \rangle$  (base) for  $L = 300$ ,  $S_{\text{tot}}/L = 81/300 = 0.27$ ,  $J = -1$ ,  $J' = 1$  for all values of  $i$ . The standard deviation of the distribution is taken as the error.

430 number. Figure 11 shows a histogram for  $L = 300$ , where the results are converged to  
 431 three digits. Note that we are hereby showing the worst case, and the distribution is even  
 432 narrower for  $L = 100, 200$ .

433 We can repeat the same procedure for a non-local quantity, namely the connected  
 434 spin-spin correlations of Eq. (9), which should depend only on the distance  $d = |l - j|$   
 435 and not on the choice of  $j$ . We average over all possible choices of  $j$ :

$$C^{\alpha\beta}[\mathbf{S}](d) := \overline{\langle \mathbf{S}_j^\alpha \cdot \mathbf{S}_{j+d}^\beta \rangle_c} = \sum_{j=1}^{N_{\text{cells}}} \langle \mathbf{S}_j^\alpha \cdot \mathbf{S}_{j+d}^\beta \rangle_c, \quad (15)$$

436 and take the standard deviation as a measure of error. Note that this quantity is inde-  
 437 pendent of  $M_{\text{tot}}$  due to the SU(2) symmetry. Since the calculation is more costly, we only  
 438 apply it to selected points. The result for  $L = 100, 200, 300$  is displayed in Fig. 12 for  
 439  $11 \leq d \leq L/4$  with the corresponding error bars. We see again that the ground state is  
 440 translationally invariant; the error bars are imperceptible for  $L = 100, 200$ .

### 441 A.3 Infinite systems: error analysis

442 For the infinite system, we check how the results of Fig. 8 depend on the bond dimension  
 443  $\chi$ . In the simulation, we let  $\chi$  grow dynamically and compute the structure factor once  
 444 the variational error becomes sufficiently small (see Ref. [45] for details). The result for  
 445  $J = -1$ ,  $J' = 1$  is displayed in Fig. 13. We see that there is no significant change around  
 446 the main peak, but there is some variation for very small  $k$ . We interpolate the result  
 447 in  $\chi^{-1}$  at selected points and find that no appreciable additional peak develops in this  
 448 region.

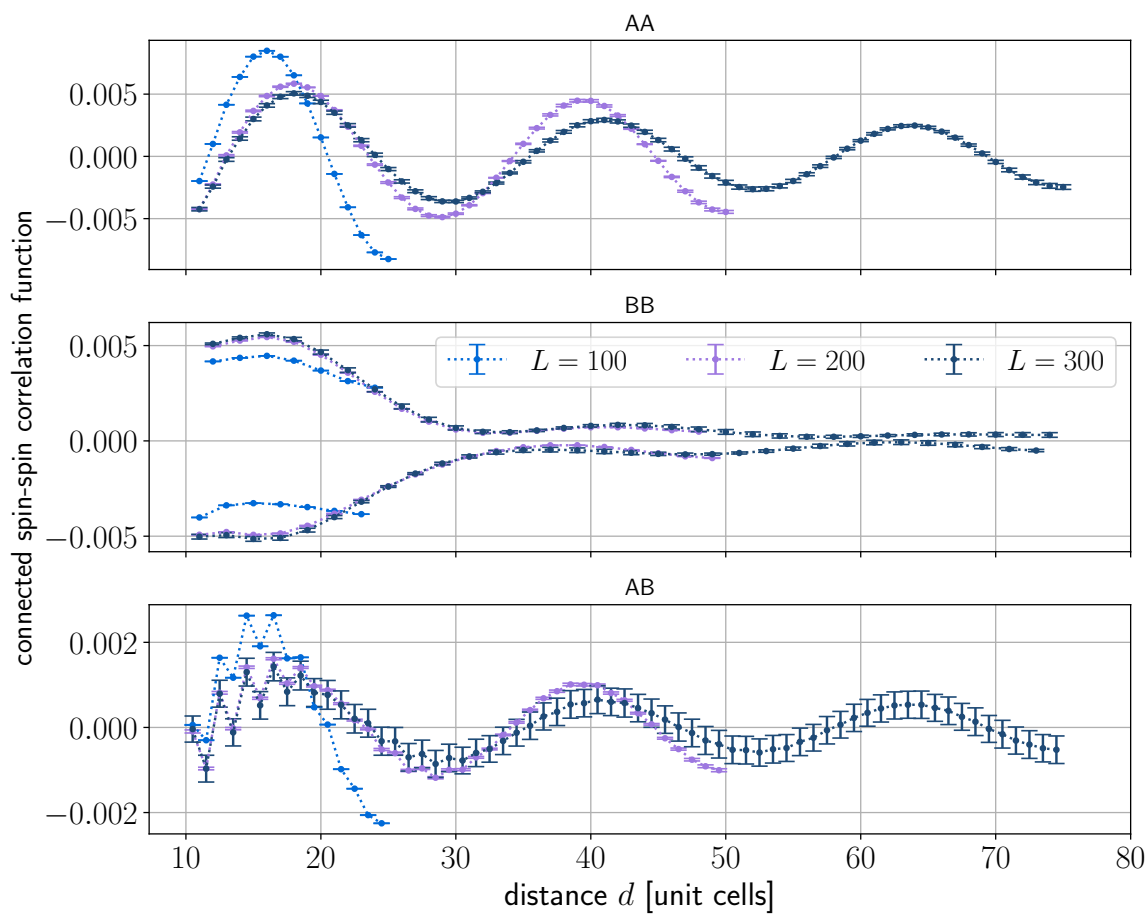


Figure 12: Connected spin-spin correlations (Eq. (15)) as a function of the distance measured in unit cells, averaged over all possible initial sites for the apical-apical (AA), basal-basal (BB) and apical-basal (AB) correlations. The standard deviation of the resulting distribution is taken as the error.

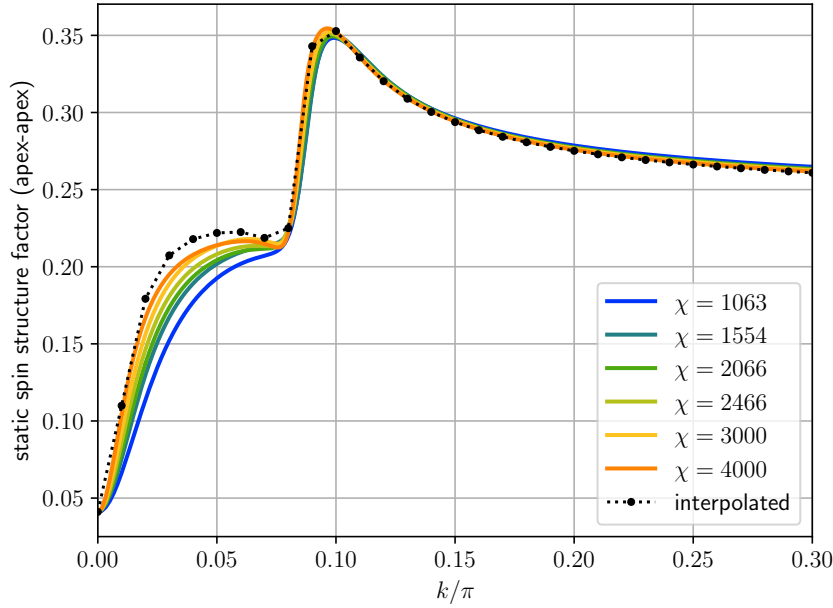


Figure 13: The static spin structure factor of Fig. 8 for  $J = -1$ ,  $J' = 1$  and different bond dimensions  $\chi$  with the U(1) spin symmetry exploited in the VUMPS algorithm. The result is linearly interpolated in  $\chi^{-1}$  at the selected black points.

#### 449 A.4 Comparison between finite and infinite systems

450 Finally, we compare the full spin-spin correlations  $\langle \mathbf{S}_j^A \cdot \mathbf{S}_{j+d}^A \rangle$  between finite and infinite  
 451 systems (see Fig. 14). We reiterate that this quantity does not depend on the choice of  
 452  $M_{\text{tot}}$ . The comparison between the curves with  $L = 100$  and  $L = 400$  indicates that  
 453 finite-size effects are still manifest for  $L = 100$  and  $d \geq 10$ .

454 The infinite-system calculation can reproduce the correlations for small distances ( $d \leq$   
 455 10) rather well even for small bond dimensions  $\chi$ . In the long-range regime, however,  
 456 any finite  $\chi$  always leads to an exponential decay and thus very large deviations from the  
 457  $L = 400$  result (which is converged w.r.t. the bond dimension).

458 Notably, however, the long wavelength of the oscillations is still reproduced. Figure 15  
 459 shows that this is almost entirely due to the z-component, so that the quantum spin spiral  
 460 manifests itself as a peak in the corresponding structure factor (see Sec. 5). This again  
 461 illustrates that both Eq. (12) and Eq. (13) can be used to demonstrate the existence of  
 462 the spiral.

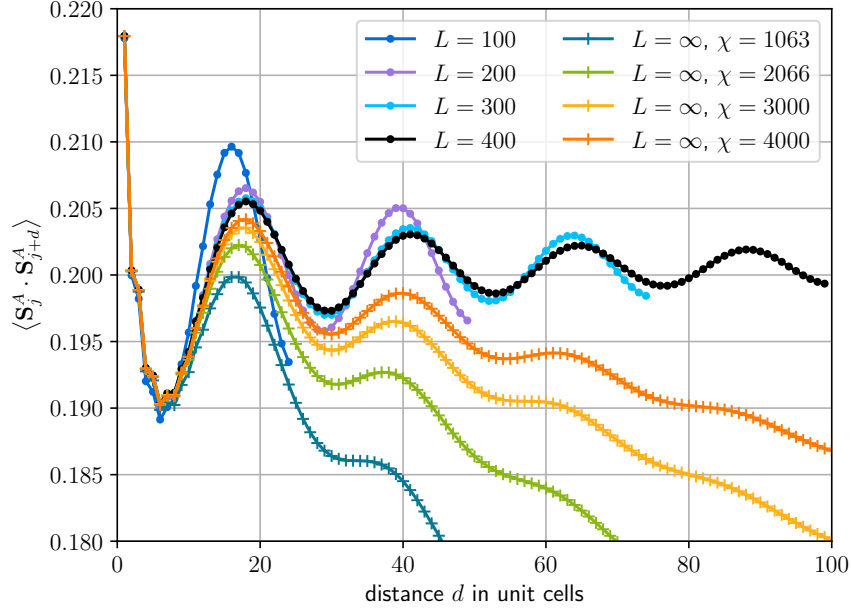


Figure 14: Comparison of the full apex-apex spin correlations for  $J = -1$ ,  $J' = 1$  between finite rings of different sizes and the infinite system (with the U(1) symmetry exploited) for various bond dimensions as a function of the distance  $d$ .

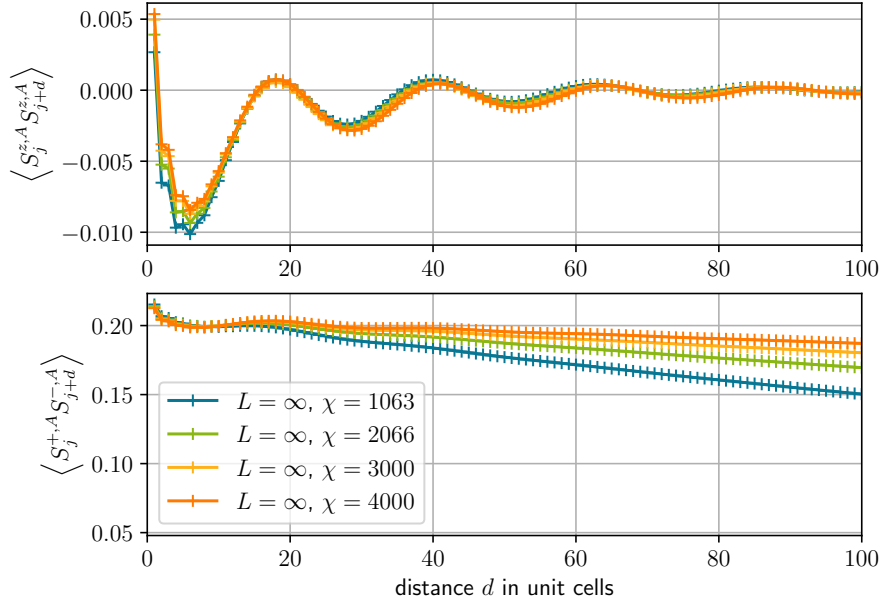


Figure 15: Individual components of the apex-apex spin correlations  $\langle S_j^{z,A} S_{j+d}^{z,A} \rangle$  (top) and  $\langle S_j^{+,A} S_{j+d}^{-,A} \rangle$  (bottom,  $S_j^{\pm,\alpha} = S_j^{x,\alpha} \pm iS_j^{y,\alpha}$ ) computed in the infinite system with U(1) symmetries exploited.

## References

- 463
- 464 [1] E. Lieb and D. Mattis, *Ordering energy levels of interacting spin systems*, Journal of  
465 Mathematical Physics **3**(4), 749 (1962).
- 466 [2] E. H. Lieb, *Two theorems on the Hubbard model*, Phys. Rev. Lett. **62**, 1201 (1989),  
467 doi:10.1103/PhysRevLett.62.1201.
- 468 [3] J.-J. Jiang, Y.-J. Liu, F. Tang, C.-H. Yang and Y.-B. Sheng, *Analytical and numerical*  
469 *studies of the one-dimensional sawtooth chain*, Physica B: Condensed Matter **463**,  
470 30 (2015), doi:<https://doi.org/10.1016/j.physb.2015.01.036>.
- 471 [4] J.-J. Jiang, F. Tang and C.-H. Yang, *Frustration induced noncollinear magnetic*  
472 *order phase in one-dimensional Heisenberg chain with alternating antiferromagnetic*  
473 *and ferromagnetic next nearest neighbor interactions*, Journal of the Physical Society  
474 of Japan **84**(12), 124710 (2015), doi:10.7566/JPSJ.84.124710, [https://doi.org/10.](https://doi.org/10.7566/JPSJ.84.124710)  
475 [7566/JPSJ.84.124710](https://doi.org/10.7566/JPSJ.84.124710).
- 476 [5] T. Yamaguchi, S.-L. Drechsler, Y. Ohta and S. Nishimoto, *Variety of order-by-*  
477 *disorder phases in the asymmetric  $J_1 - J_2$  zigzag ladder: From the delta chain to the*  
478  *$J_1 - J_2$  chain*, Phys. Rev. B **101**, 104407 (2020), doi:10.1103/PhysRevB.101.104407.
- 479 [6] M. Steinbrecher, R. Rausch, K. T. That, J. Hermenau, A. A. Khajetoorians, M. Pot-  
480 thoff, R. Wiesendanger and J. Wiebe, *Non-collinear spin states in bottom-up fabri-*  
481 *cated atomic chains*, Nature communications **9**(1), 1 (2018).
- 482 [7] M. Thesberg and E. S. Sørensen, *General quantum fidelity susceptibilities for the*  
483  *$J_1$ - $J_2$  chain*, Phys. Rev. B **84**, 224435 (2011), doi:10.1103/PhysRevB.84.224435.
- 484 [8] T. Masuda, A. Zheludev, B. Roessli, A. Bush, M. Markina and A. Vasiliev, *Spin*  
485 *waves and magnetic interactions in  $LiCu_2O_2$* , Phys. Rev. B **72**, 014405 (2005),  
486 doi:10.1103/PhysRevB.72.014405.
- 487 [9] S. Park, Y. J. Choi, C. L. Zhang and S.-W. Cheong, *Ferroelectric-*  
488 *ity in an  $s = 1/2$  chain cuprate*, Phys. Rev. Lett. **98**, 057601 (2007),  
489 doi:10.1103/PhysRevLett.98.057601.
- 490 [10] Y. Naito, K. Sato, Y. Yasui, Y. Kobayashi, Y. Kobayashi and M. Sato, *Ferroelectric*  
491 *transition induced by the incommensurate magnetic ordering in  $LiCuVO_4$* , Journal  
492 of the Physical Society of Japan **76**(2), 023708 (2007), doi:10.1143/JPSJ.76.023708,  
493 <https://doi.org/10.1143/JPSJ.76.023708>.
- 494 [11] Y. Yasui, M. Sato and I. Terasaki, *Multiferroic behavior in the quasi-one-dimensional*  
495 *frustrated spin-1/2 system  $PbCuSO_4(OH)_2$  with  $CuO_2$  ribbon chains*, Journal of the  
496 Physical Society of Japan **80**(3), 033707 (2011), doi:10.1143/JPSJ.80.033707, [https:](https://doi.org/10.1143/JPSJ.80.033707)  
497 [//doi.org/10.1143/JPSJ.80.033707](https://doi.org/10.1143/JPSJ.80.033707).
- 498 [12] C. Papatriantafyllopoulou, E. E. Moushi, G. Christou and A. J. Tasiopoulos, *Filling*  
499 *the gap between the quantum and classical worlds of nanoscale magnetism: giant*  
500 *molecular aggregates based on paramagnetic 3d metal ions*, Chemical Society Reviews  
501 **45**(6), 1597 (2016).
- 502 [13] A. J. Tasiopoulos, A. Vinslava, W. Wernsdorfer, K. A. Abboud and G. Chris-  
503 tou, *Giant single-molecule magnets: A  $Mn_8$  torus and its supramolecu-*  
504 *lar nanotubes*, Angewandte Chemie International Edition **43**(16), 2117 (2004),



- 505 doi:<https://doi.org/10.1002/anie.200353352>, <https://onlinelibrary.wiley.com/doi/pdf/10.1002/anie.200353352>.  
506
- 507 [14] A. Vinslava, A. J. Tasiopoulos, W. Wernsdorfer, K. A. Abboud and G. Christou, *Molecules at the quantum–classical nanoparticle interface: Giant Mn70 single-molecule magnets of  $\sim 4$  nm diameter*, *Inorganic Chemistry* **55**(7), 3419 (2016), doi:10.1021/acs.inorgchem.5b02790, PMID: 26859234, <https://doi.org/10.1021/acs.inorgchem.5b02790>.  
508  
509  
510  
511
- 512 [15] H. F. Schurkus, D. Chen, M. J. O’Rourke, H.-P. Cheng and G. K.-L. Chan, *Exploring the magnetic properties of the largest single-molecule magnets*, *The Journal of Physical Chemistry Letters* **11**(10), 3789 (2020), doi:10.1021/acs.jpcllett.0c00020, PMID: 32331500, <https://doi.org/10.1021/acs.jpcllett.0c00020>.  
513  
514  
515
- 516 [16] F. Monti and A. Sütő, *Spin-1/2 Heisenberg model on  $\Delta$  trees*, *Physics Letters A* **156**(3), 197 (1991), doi:[https://doi.org/10.1016/0375-9601\(91\)90937-4](https://doi.org/10.1016/0375-9601(91)90937-4).  
517
- 518 [17] C. Ruiz-Pérez, M. Hernández-Molina, P. Lorenzo-Luis, F. Lloret, J. Cano and M. Julve, *Magnetic coupling through the carbon skeleton of malonate in two polymorphs of  $\{[Cu(bpy)(H_2O)][Cu(bpy)(mal)(H_2O)]\}(ClO_4)_2$  ( $H_2mal$  = malonic acid;  $bpy$  = 2,2’-bipyridine)*, *Inorganic Chemistry* **39**(17), 3845 (2000).  
519  
520  
521
- 522 [18] T. Tonegawa and M. Kaburagi, *Ground-state properties of an  $s=1/2$   $\Delta$ -chain with ferro- and antiferromagnetic interactions*, *Journal of Magnetism and Magnetic Materials* **272-276**, 898 (2004), doi:<https://doi.org/10.1016/j.jmmm.2003.11.367>, Proceedings of the International Conference on Magnetism (ICM 2003).  
523  
524  
525
- 526 [19] M. Kaburagi, T. Tonegawa and M. Kang, *Ground state phase diagrams of an anisotropic spin-1/2  $\Delta$ -chain with ferro- and antiferromagnetic interactions*, *Journal of applied physics* **97**(10), 10B306 (2005).  
527  
528
- 529 [20] Y. Inagaki, Y. Narumi, K. Kindo, H. Kikuchi, T. Kamikawa, T. Kunimoto, S. Okubo, H. Ohta, T. Saito, M. Azuma, M. Takano, H. Nojiri *et al.*, *Ferro-antiferromagnetic delta-chain system studied by high field magnetization measurements*, *Journal of the Physical Society of Japan* **74**(10), 2831 (2005), doi:10.1143/JPSJ.74.2831, <https://doi.org/10.1143/JPSJ.74.2831>.  
530  
531  
532  
533
- 534 [21] D. Sen, B. S. Shastry, R. E. Walstedt and R. Cava, *Quantum solitons in the sawtooth lattice*, *Phys. Rev. B* **53**, 6401 (1996), doi:10.1103/PhysRevB.53.6401.  
535
- 536 [22] T. Nakamura and K. Kubo, *Elementary excitations in the  $\Delta$  chain*, *Phys. Rev. B* **53**, 6393 (1996), doi:10.1103/PhysRevB.53.6393.  
537
- 538 [23] J. Schulenburg, A. Honecker, J. Schnack, J. Richter and H.-J. Schmidt, *Macroscopic magnetization jumps due to independent magnons in frustrated quantum spin lattices*, *Phys. Rev. Lett.* **88**, 167207 (2002), doi:10.1103/PhysRevLett.88.167207.  
539  
540
- 541 [24] S. Blundell and M. Núñez-Regueiro, *Quantum topological excitations: from the sawtooth lattice to the Heisenberg chain*, *The European Physical Journal B-Condensed Matter and Complex Systems* **31**(4), 453 (2003).  
542  
543
- 544 [25] M. E. Zhitomirsky and A. Honecker, *Magnetocaloric effect in one-dimensional antiferromagnets*, *Journal of Statistical Mechanics: Theory and Experiment* **2004**(07), P07012 (2004), doi:10.1088/1742-5468/2004/07/p07012.  
545  
546

- 547 [26] J. Richter, J. Schulenburg, A. Honecker, J. Schnack and H.-J. Schmidt, *Exact*  
548 *eigenstates and macroscopic magnetization jumps in strongly frustrated spin lat-*  
549 *tices*, Journal of Physics: Condensed Matter **16**(11), S779 (2004), doi:10.1088/0953-  
550 8984/16/11/029.
- 551 [27] J. Richter, *Localized-magnon states in strongly frustrated quantum spin lattices*, Low  
552 Temperature Physics **31**(8), 695 (2005).
- 553 [28] O. Derzhko, J. Schnack, D. V. Dmitriev, V. Y. Krivnov and J. Richter, *Flat-band*  
554 *physics in the spin-1/2 sawtooth chain*, The European Physical Journal B **93**(8), 1  
555 (2020).
- 556 [29] L. Heinze, H. O. Jeschke, I. I. Mazin, A. Metavitsiadis, M. Reehuis, R. Feyerherm,  
557 J.-U. Hoffmann, M. Bartkowiak, O. Prokhnenko, A. U. B. Wolter, X. Ding, V. S. Zapf  
558 *et al.*, *Magnetization process of atacamite: A case of weakly coupled  $s = 1/2$  sawtooth*  
559 *chains*, Phys. Rev. Lett. **126**, 207201 (2021), doi:10.1103/PhysRevLett.126.207201.
- 560 [30] A. Baniodeh, N. Magnani, Y. Lan, G. Buth, C. E. Anson, J. Richter, M. Affronte,  
561 J. Schnack and A. K. Powell, *High spin cycles: topping the spin record for a single*  
562 *molecule verging on quantum criticality*, npj Quantum Materials **3**(1), 1 (2018).
- 563 [31] S. Furukawa, M. Sato, S. Onoda and A. Furusaki, *Ground-state phase diagram of a*  
564 *spin- $\frac{1}{2}$  frustrated ferromagnetic XXZ chain: Haldane dimer phase and gapped/gapless*  
565 *chiral phases*, Phys. Rev. B **86**, 094417 (2012), doi:10.1103/PhysRevB.86.094417.
- 566 [32] C. E. Agrapidis, S.-L. Drechsler, J. van den Brink and S. Nishimoto, *Coexistence of*  
567 *valence-bond formation and topological order in the Frustrated Ferromagnetic  $J_1$ - $J_2$*   
568 *Chain*, SciPost Phys. **6**, 19 (2019), doi:10.21468/SciPostPhys.6.2.019.
- 569 [33] O. Derzhko and J. Richter, *Universal low-temperature behavior of frustrated quantum*  
570 *antiferromagnets in the vicinity of the saturation field*, Eur. Phys. J. B **52**, 23 (2006),  
571 doi:10.1140/epjb/e2006-00273-y.
- 572 [34] O. Derzhko, J. Richter and M. Maksymenko, *Strongly correlated flat-band systems:*  
573 *The route from Heisenberg spins to Hubbard electrons*, International Journal of Mod-  
574 ern Physics B **29**, 1530007 (2015), doi:10.1142/S0217979215300078.
- 575 [35] J. Richter, V. Ohanyan, J. Schulenburg and J. Schnack, *Electric field driven flat bands:*  
576 *Enhanced magnetoelectric and electrocaloric effects in frustrated quantum magnets*,  
577 Phys. Rev. B **105**, 054420 (2022), doi:10.1103/PhysRevB.105.054420.
- 578 [36] V. Y. Krivnov, D. V. Dmitriev, S. Nishimoto, S.-L. Drechsler and J. Richter, *Delta*  
579 *chain with ferromagnetic and antiferromagnetic interactions at the critical point*,  
580 Phys. Rev. B **90**, 014441 (2014), doi:10.1103/PhysRevB.90.014441.
- 581 [37] D. V. Dmitriev, V. Y. Krivnov, J. Richter and J. Schnack, *Thermodynamics of a*  
582 *delta chain with ferromagnetic and antiferromagnetic interactions*, Phys. Rev. B **99**,  
583 094410 (2019), doi:10.1103/PhysRevB.99.094410.
- 584 [38] S. R. White, *Density matrix formulation for quantum renormalization groups*, Phys.  
585 Rev. Lett. **69**, 2863 (1992), doi:10.1103/PhysRevLett.69.2863.
- 586 [39] U. Schollwöck, *The density-matrix renormalization group in the*  
587 *age of matrix product states*, Annals of Physics **326**, 96 (2011),  
588 doi:https://doi.org/10.1016/j.aop.2010.09.012.

- 589 [40] J. Eisert, M. Cramer and M. B. Plenio, *Colloquium: Area laws for the entanglement*  
590 *entropy*, Rev. Mod. Phys. **82**, 277 (2010), doi:10.1103/RevModPhys.82.277.
- 591 [41] C. Hubig, I. P. McCulloch, U. Schollwöck and F. A. Wolf, *Strictly single-site*  
592 *DMRG algorithm with subspace expansion*, Phys. Rev. B **91**, 155115 (2015),  
593 doi:10.1103/PhysRevB.91.155115.
- 594 [42] I. P. McCulloch, *From density-matrix renormalization group to matrix product states*,  
595 Journal of Statistical Mechanics: Theory and Experiment **2007**(10), P10014 (2007),  
596 doi:10.1088/1742-5468/2007/10/p10014.
- 597 [43] S. Keller and M. Reiher, *Spin-adapted matrix product states and operators*, The  
598 Journal of Chemical Physics **144**(13), 134101 (2016), doi:10.1063/1.4944921, <https://doi.org/10.1063/1.4944921>.  
599
- 600 [44] H. T. Johansson and C. Forssén, *Fast and accurate evaluation of Wigner  $3j$ ,  $6j$ , and*  
601  *$9j$  symbols using prime factorization and multiword integer arithmetic*, SIAM Journal  
602 on Scientific Computing **38**(1), A376 (2016), doi:10.1137/15M1021908, <https://doi.org/10.1137/15M1021908>.  
603
- 604 [45] V. Zauner-Stauber, L. Vanderstraeten, M. T. Fishman, F. Verstraete and J. Haegeman,  
605 *Variational optimization algorithms for uniform matrix product states*, Phys.  
606 Rev. B **97**, 045145 (2018), doi:10.1103/PhysRevB.97.045145.
- 607 [46] L. Vanderstraeten, J. Haegeman and F. Verstraete, *Tangent-space methods*  
608 *for uniform matrix product states*, SciPost Phys. Lect. Notes p. 7 (2019),  
609 doi:10.21468/SciPostPhysLectNotes.7.
- 610 [47] R. Rausch and M. Peschke, *Topological phases arising from attractive interaction and*  
611 *pair hopping in the extended Hubbard model*, New Journal of Physics **22**(7), 073051  
612 (2020), doi:10.1088/1367-2630/ab9c65.
- 613 [48] B. Nachtergaele and S. Starr, *Ferromagnetic Lieb-Mattis theorem*, Phys. Rev. Lett.  
614 **94**, 057206 (2005), doi:10.1103/PhysRevLett.94.057206.
- 615 [49] J. Schulenburg, *spinpack 2.56*, Magdeburg University (2017).